STREAMLINE.
OPTIMIZE.
TRUST.

ADAPTIVO | LINACVIEW | DOSEVIEW | PIPSPRO | QA PILOT | IMSURE | STRUCTSURE AI QA

COMPLETE INTEGRATED QA

STANDARD IMAGING®

CLICK HERE TO LEARN MORE

Modulating ultrasound contrast generation from injectable nanodroplets for proton range verification by varying the degree of superheat

Sophie V. Heymans*
Department of Physics, KU Leuven Campus Kulak, Kortrijk, Belgium

Bram Carlier*
Department of Oncology, KU Leuven, Leuven, Belgium
Molecular Small Animal Imaging Center, KU Leuven, Leuven, Belgium

Yosra Toumia
Department of Chemical Sciences and Technology, University of Rome Tor Vergata, Rome, Italy

Sjoerd Nooijens and Marcus Ingram
Department of Cardiovascular Sciences, KU Leuven, Leuven, Belgium

Andrea Giammanco and Emiliano d'Agostino
DoseVue, Diepenbeek, Belgium

Wouter Crijns
Department of Oncology, KU Leuven, Leuven, Belgium

Alexander Bertrand
Department of Electrical Engineering (ESAT), KU Leuven, Leuven, Belgium

Gaio Paradossi
Department of Chemical Sciences and Technology, University of Rome Tor Vergata, Rome, Italy

Uwe Himmelreich
Molecular Small Animal Imaging Center, KU Leuven, Leuven, Belgium
Department of Imaging & Pathology, KU Leuven, Leuven, Belgium

Jan D'hooge
Department of Cardiovascular Sciences, KU Leuven, Leuven, Belgium

Edmond Sterpin†
Department of Oncology, KU Leuven, Leuven, Belgium

Koen Van Den Abeele†,a)
Department of Physics, KU Leuven Campus Kulak, Kortrijk, Belgium

(Received 26 September 2020; revised 21 January 2021; accepted for publication 8 February 2021; published 11 March 2021)

Purpose: Despite the physical benefits of protons over conventional photon radiation in cancer treatment, range uncertainties impede the ability to harness the full potential of proton therapy. While monitoring the proton range *in vivo* could reduce the currently adopted safety margins, a routinely applicable range verification technique is still lacking. Recently, phase-change nanodroplets were proposed for proton range verification, demonstrating a reproducible relationship between the proton range and generated ultrasound contrast after radiation-induced vaporization at 25°C. In this study, previous findings are extended with proton irradiations at different temperatures, including the physiological temperature of 37°C, for a novel nanodroplet formulation. Moreover, the potential to modulate the linear energy transfer (LET) threshold for vaporization by varying the degree of superheat is investigated, where the aim is to demonstrate vaporization of nanodroplets directly by primary protons.

Methods: Perfluorobutane nanodroplets with a shell made of polyvinyl alcohol (PVA-PFB) or 10,12-pentacosadyinoic acid (PCDA-PFB) were dispersed in polyacrylamide hydrogels and irradiated with 62 MeV passively scattered protons at temperatures of 37°C and 50°C. Nanodroplet transition into echogenic microbubbles was assessed using ultrasound imaging (gray value and attenuation analysis) and optical images. The proton range was measured independently and compared to the generated contrast.

Results: Nanodroplet design proved crucial to ensure thermal stability, as PVA-shelled nanodroplets dramatically outperformed their PCDA-shelled counterpart. At body temperature, a uniform radiation response proximal to the Bragg peak is attributed to nuclear reaction products interacting with PVA-PFB nanodroplets, with the 50% drop in ultrasound contrast being 0.17 mm ± 0.20 mm

(mean ± standard deviation) in front of the proton range. Also at 50°C, highly reproducible ultrasound contrast profiles were obtained with shifts of −0.74 mm ± 0.09 mm (gray value analysis), −0.86 mm ± 0.04 mm (attenuation analysis) and −0.64 mm ± 0.29 mm (optical analysis). Moreover, a strong contrast enhancement was observed near the Bragg peak, suggesting that nanodroplets were sensitive to primary protons.

Conclusions: By varying the degree of superheat of the nanodroplets' core, one can modulate the intensity of the generated ultrasound contrast. Moreover, a submillimeter reproducible relationship between the ultrasound contrast and the proton range was obtained, either indirectly via the visualization of secondary reaction products or directly through the detection of primary protons, depending on the degree of superheat. The potential of PVA-PFB nanodroplets for *in vivo* proton range verification was confirmed by observing a reproducible radiation response at physiological temperature, and further studies aim to assess the nanodroplets' performance in a physiological environment. Ultimately, cost-effective online or offline ultrasound imaging of radiation-induced nanodroplet vaporization could facilitate the reduction of safety margins in treatment planning and enable adaptive proton therapy. [https://doi.org/10.1002/mp.14778]

Key words: nanodroplets, proton therapy, range verification, ultrasound

1. INTRODUCTION

Proton dose deposition profiles are characterized by a low entrance dose and a narrow Bragg peak, followed by a sharp distal dose fall-off. These physical features have provided a strong impetus for the development of proton centers for cancer treatment in the past decades.[1] However, even with the availability of powerful Monte Carlo engines allowing the development of highly accurate treatment plans *a priori*, the exact proton range *in vivo* remains unknown.[2] Indeed, considerable range uncertainties arise from the ambiguous conversion of Houndsfield units (HU) to stopping powers, patient motion, setup inaccuracies, and anatomical changes over the course of the treatment.[2] This is accounted for by the addition of substantial safety margins on the original treatment plan and the choice of suboptimal beam arrangements, preventing full exploitation of the ballistic advantage of protons.[3–5] To solve this problem, several *in vivo* range verification techniques have been investigated. PET imaging detects coincident gamma rays emitted by certain isotopes produced by nuclear reactions of the proton beam with atomic constituents of the tissue being irradiated.[6–9] However, complex models and simulations are required to relate the obtained PET signals to the actual proton range and limited accuracy is achieved.[3,10] Prompt gamma imaging has the potential to provide real-time range feedback by detecting the prompt gamma radiation released from similar nuclear interactions,[11–13] but the lack of suitable and cost-effective detectors has prevented its translation to standard clinical practice.[2,14] Recently, ionoacoustic imaging has emerged as a novel approach to determine the proton range by probing the ultrasound signals arising from the thermo-elastic tissue expansions induced by localized dose deposition at the Bragg peak.[15–19] While the Bragg peak location was detected in phantom experiments with submillimeter resolution, the technique is limited to pulsed proton accelerators given its transient nature.[20,21] Finally, radiation-induced changes of tissue properties detected by magnetic resonance imaging can be used as a post-treatment range verification approach as demonstrated for spinal and liver tissues.[22,23] However, an important constraint is that those changes occur weeks after irradiation, preventing the compensation of range errors over the course of the treatment.[22] In general, due to the aforementioned limitations, none of the presented technologies are routinely adopted in the clinic.[24]

The European Horizon 2020 project "Amphora" recently revisited superheated emulsions as an alternative means to measure the proton range.[25] Superheated emulsions typically comprise micrometer or millimeter-sized drops dispersed in an immiscible aqueous matrix.[26] Owing to the absence of heterogeneous nucleation sites, these droplets can be operated at temperatures above their boiling point, in a metastable superheated state, without vaporizing.[27,28] However, when charged particles with sufficient linear energy transfer (LET) traverse these droplets, small vapor embryos are created that can eventually trigger complete vaporization of the drops into gaseous bubbles as described by Seitz's thermal spike theory.[29–31] These highly echogenic bubbles can then be detected via optical, acoustic, or volume measurements.[26,32] For the past half century, this principle has been exploited by bubble chambers and superheated drop detectors in a variety of fields ranging from radiation spectrometry and dosimetry to space applications and dark matter search.[33–37] Furthermore, it was envisioned for *in vivo* applications two decades ago.[38]

To apply this concept to *in vivo* noninvasive radiation dosimetry and proton range verification, the aforementioned emulsions were downscaled to phase-change nanodroplets and stabilized by a lipidic shell.[25] This was facilitated by recent developments in the field of ultrasound imaging and therapy,[39–42] which led to the emergence of several injectable superheated nanodroplet formulations able to provide ultrasound contrast on demand when triggered by acoustic[43,44] or optical[45] sources. A first proof-of-concept study was recently

performed with nanodroplets made of a 10,12-pentacosadiynoic acid shell encapsulating a liquid decafluorobutane core (PCDA-PFB, boiling point = −2°C),[44] demonstrating radiation-induced vaporization in a proton beam at room temperature (25°C).[25] Moreover, a highly reproducible (<1 mm) relationship between the proton range and the generated ultrasound contrast was observed, thereby disclosing the potential of superheated nanodroplets for ultrasound-guided *in vivo* range verification. The presence of a shift was explained by the LET threshold for perfluorobutane droplets at 25°C (370 keV/μm) predicted by the thermal spike theory[26] (Fig. 1). This indicates that only secondary recoil nuclei generated by nonelastic interactions carried sufficient LET to trigger droplet vaporization, harnessing only a small fraction of the radiation for ultrasound signal generation.

In this contribution, those previous findings are extended by exploring the potential to modulate I) the overall ultrasound contrast generation and II) its relationship to the proton range, by varying the degree of superheat, *s*, defined as:

$$s = \frac{T - T_b}{T_c - T_b}$$

with T the ambient temperature and T_b and T_c the boiling and critical temperature of the nanodroplets' liquid core, respectively. Due to the limited thermal stability of the PCDA-PFB nanodroplets, the lipidic shell was replaced by a more resistant polyvinyl alcohol (PVA) shell for the experiments in this study. First, the radiation response of these PVA-PFB nanodroplets was evaluated in phantoms at physiological temperature, taking the next step toward the eventual *in vivo* application. Afterwards, irradiations at 50°C were performed to investigate whether nanodroplet vaporization induced by the primary proton beam could be achieved, as predicted by the radiation-induced nucleation theory[26,31] (Fig. 1). Ultrasound imaging was employed to evaluate nanodroplet vaporization profiles, which were subsequently compared to the proton range. Finally, the observations at different degrees of superheat were compared and explained by the theory of radiation-induced nucleation of superheated emulsions.

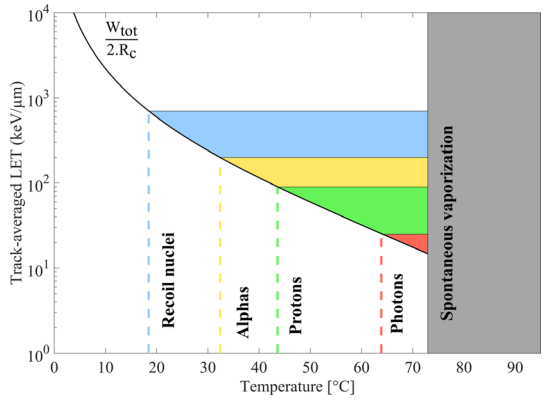

FIG. 1. Linear energy transfer (LET) threshold, obtained from the thermal spike theory as the ratio between the nucleation energy (W_{tot}) and twice the critical radius (R_c), for perfluorobutane droplets as a function of temperature. Shaded areas highlight the temperature zones where droplets are sensitized to the respective particles. Above 76°C, the superheated metastable state can no longer exist and spontaneous vaporization takes place. [Color figure can be viewed at wileyonlinelibrary.com]

2. MATERIALS AND METHODS

2.A. Nanodroplet synthesis and size distribution

Unless described otherwise, all chemicals were obtained from Sigma-Aldrich (Darmstadt, Germany). The PVA-PFB nanodroplet preparation was performed as follows. First, 1 g of fully hydrolyzed PVA was dissolved in 50 ml Milli-Q water at 80°C. After complete dissolution, heating was stopped and 95 mg of sodium periodate was added and stirred for 1 h to oxidize the PVA chains. Separately, an empty glass vial sealed with a rubber septum was immersed in liquid nitrogen and injected with gaseous perfluorobutane (F2 Chemicals Ltd, United Kingdom), which immediately condensed, for a few seconds. Afterwards, 5 ml of the oxidized PVA solution was added to this vial and the mixture was sonicated in an ice-cold water bath (Elmasonic X_TRA 30H, Elma Schmidbauer GmbH, Germany) for 15 min. After an additional 1 h incubation at 4°C, the nanodroplet solution was washed by a two-step centrifugation. First, the glass vial was centrifuged for 5 min at 1200 g (Thermo Scientific SL 16, Thermo Electron LET GmbH, Germany). The supernatant was transferred to a plastic Falcon tube and underwent a second centrifugation at 4700 g for another 5 min. Finally, both pellets were resuspended in Milli-Q water and combined. PCDA-PFB nanodroplets were prepared as described previously.[25,44] The resulting nanodroplet solutions were stored in the fridge and used within 1 week after preparation.

Dynamic light scattering (NanoBrook Omni, Brookhaven Instruments, Corporation, NY) was used to measure the PVA-PFB nanodroplet size distribution, and yielded an intensity-weighted median diameter of 799 nm ± 25 nm (n = 7, repetitions over two different vials) and a polydispersity index of 0.3 ± 0.01. The PCDA-PFB nanodroplets have an intensity-weighted median diameter of 842 nm ± 12 nm (n = 4) and a polydispersity index of 0.25 ± 0.02.[25]

2.B. Phantom preparation

Phantoms were prepared in bespoke containers of inner dimensions $L = 38$ mm, $W = 24$ mm and $H = 25$ mm. First, the 30% acrylamide–bisacrylamide (Am/Bis) stock solution (29:1, Bio-Rad Laboratories NV, Belgium) was diluted to 5% in Milli-Q water and degassed via sonication. Next, 22.2 ml of this solution was poured into the phantom container and mixed with 570 μl of 8.5% (w/v) ammonium persulfate in Milli-Q water. Afterwards, the required volume of nanodroplets was added to achieve a final perfluorobutane concentration of 25 μM in the phantom. Perfluorobutane concentration of the nanodroplet solution was previously

quantified using NMR spectroscopy (400 MHz Avance II, Bruker Biospin GmbH, Rheinstetten, Germany). Then, 28.5 µl of TEMED was added and the mixture was homogenized, before allowing gelation for 30 min at room temperature. Finally, the phantoms were heated to the desired temperature in a water bath, just prior to irradiation (Fig. 2).

2.C. Irradiation protocol

2.C.1. Phantom irradiation

Proton irradiations were performed at the Centre de Ressources du Cyclotron (UCLouvain, Louvain-la-Neuve, Belgium), equipped with a cyclotron (CYCLONE 110) producing a passively scattered proton beam with a nominal energy of 62 MeV. Phantoms were placed in a heated water tank equipped with temperature control (±0.5°C) and aligned in the proton beam (Fig. 2). The orange pipes depicted in the irradiation setup are metallic heating elements, connected to a temperature controller. The proton beam was collimated by a 4 cm diameter brass aperture and covered the entire phantom cross section. The phantoms were heated to two temperatures, 37°C in order to mimic physiological conditions, and 50°C aiming at nanodroplet vaporization by the primary proton beam. At 37°C, six PVA-PFB phantoms received each a dose of 10 Gy at a dose rate of 2 Gy/min (doses and dose rates are reported at the Bragg peak location), while four others were irradiated at 50°C (dose rate of 4 Gy/min): three phantoms received a dose of 10 Gy and one phantom received 2 Gy. For all irradiations, the beam energy was 62 MeV. Control phantoms underwent the same temperature conditions, but were not irradiated. Additionally, PCDA-PFB phantoms were irradiated at 37°C, but were not included for further analysis because the radiation response was indistinguishable from the initial background.

2.C.2. Absolute range measurement

The dose deposition profile of 62 MeV protons was measured by scanning a diode (model PR60020, PTW, Freiburg, Germany) by steps of 1 mm parallel to the beam direction in a water tank (entrance window of 23 µm polyethylene terephthalate), with a 3 mm thick polyvinyl chloride plate positioned in front, to mimic the entrance wall of the water tank used for the phantom irradiations. The range was determined as the distal point where the dose drops to 80% of the peak dose,[4] R_{80}, and obtained by fitting the depth-dose profile to an analytical approximation of the Bragg curve.[46] The impact of the phantom container wall (1.5 mm plexiglas) on the proton range was simulated with TRIM.[47] To account for the different density of polyacrylamide aqueous phantoms compared to water, rectangular Gafchromic EBT3 films (15 by 54 mm) were immersed in water and polyacrylamide phantoms at room temperature (n = 3 and 4, respectively), with an angle of 32° relative to the beam direction (to prevent in-film slowing down of the protons). Films were converted to dose[48] and the relative range difference between water and polyacrylamide was obtained after correcting for quenching effects at the Bragg peak location, following the procedure described by Fiorini et al.[49]

2.D. Data acquisition

Ultrasound images of the phantoms were acquired just prior to and immediately after proton irradiation (or immersion in a heated water bath for control phantoms) by means

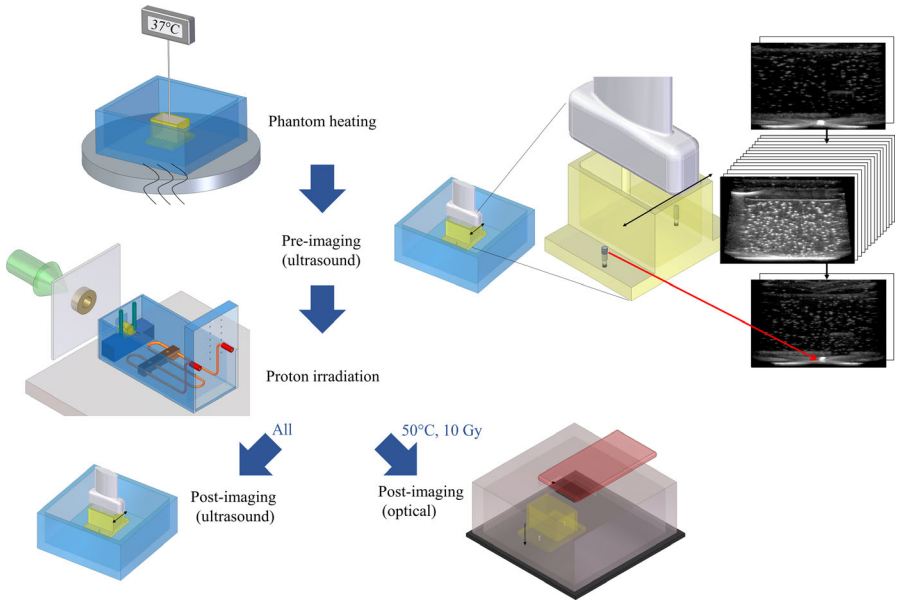

FIG. 2. Flowchart of the experimental protocol. After preparation, the phantoms were immersed in a water bath equipped with temperature control until they reached the intended temperature (37°C or 50°C). Then, all phantoms were imaged with an ultrasound scanner before being irradiated with 62 MeV protons. Afterwards, ultrasound images of all phantoms were acquired again, and optical images of phantoms that were irradiated at 50°C (10 Gy) were taken from the top with a mobile phone camera. [Color figure can be viewed at wileyonlinelibrary.com]

of an ultrasound research scanner (DiPhAS, Fraunhofer IBMT, Germany). The system was connected to a 7.5 MHz linear array (L7-Xtech, Vermon, France) mounted on a 1D linear stage to scan the phantoms parallel to the proton beam. Plane wave, low acoustic pressure imaging was adopted in order to prevent acoustic droplet vaporization. The axial and lateral resolution of the DiPhAS system was 0.20 and 0.63 mm, respectively, as determined by the full width at half maximum (FWHM) of microbubble point scatterers.

In order to match the ultrasound images of the phantom to an absolute position, external fiducials (M2 screws) were incorporated in the phantom containers, as shown in the magnification in Fig. 2. Phantom scanning consisted of acquiring two frames of the metallic screw on the front side first, then up to 20 parallel images of the phantom across its width, and finally two frames of the metallic screw on the back side.

Additionally, for the three phantoms irradiated at 50°C that received a dose of 10 Gy, three optical images per phantom were captured with a smartphone camera (12 million pixels, Iphone 8, Apple Inc., United States) in a dedicated light box (Fig. 2). The pictures were acquired 1 day after the experiment.

2.E. Data analysis

2.E.1. Ultrasound gray value analysis

First, a region of interest (ROI) was determined in the ultrasound images to exclude reflections from the phantom walls and surface, as shown in Fig. 3(a). Then, gray value profiles (representative of the microbubble density) were extracted in the ultrasound lateral direction (parallel to the proton beam) by averaging the gray values across the image depth. The obtained profiles were further averaged over the different image slices (approximately 20 per phantom). The 50% drop in gray value was extracted from the profiles as described previously,[25] by applying a moving average filter, followed by a derivative filter to locate the slope maximum, in the transition zone, and finally taking the midpoint between the highest and lowest gray values in a 3.6-mm-wide interval surrounding the position of maximum slope [Fig. 3(a)]. The intensity-weighted center-of-mass of the fiducials was used to relate the image coordinates to an absolute position. The absolute proton range was compared to the ultrasound contrast by calculating the difference between the R_{80} value and the 50% drop in gray value. Results are presented as mean±standard deviation, describing interphantom variability.

2.E.2. Ultrasound attenuation analysis

In the presence of a large microbubble density, the actual ultrasound contrast could not be determined accurately along the complete phantom depth due to acoustic shadowing.[50,51] While both the scattering (hence the image gray value) and the attenuation coefficient (expressed in dB/cm) are proportional to the microbubble concentration,[52] estimating the attenuation coefficient might prove more robust against acoustic shadowing artifacts. We therefore modified a recently described approach to evaluate tissue attenuation,[53] as an alternative analysis for the phantoms irradiated at 50°C, where non-negligible acoustic shadowing was observed. The methodology involves fitting a known attenuation model to ultrasound beamformed radiofrequency data in the frequency domain. The magnitude spectrum of the backscattered signal can be modelled as:

$$|S(f,z)| = G'|P(f)|A(f,z)B(f,z).$$

In this expression, f is the frequency and z is the ultrasound axial depth. $|P(f)|$ is the impulse response or pulse-echo transfer function of the ultrasound array, which can be determined by a pulse-echo reflector measurement, and G' is an unknown gain factor. The impulse response variation across the different transducer elements was considered negligible. Diffraction effects were neglected as plane wave imaging was employed[54] and the attenuation coefficient was estimated along a line, assuming a 1D propagation. $A(f,z)$ denotes the attenuation of the medium and can be described by a function exponentially decaying with depth: $A(f,z) = e^{-2\alpha(f)z}$, where $\alpha(f)$ is the frequency-dependent attenuation coefficient and the factor of two accounts for the two-way travel of the ultrasound wave in the sample. Finally, $B(f,z)$ represents the backscatter coefficient of the medium and was assumed independent of frequency and depth for simplicity, hence $B(f,z) = B_0$. Although the assumption of frequency independence is not strictly correct for bubbly media,[55] it has been shown to hold at frequencies above resonance.[56,57] The equation can be linearized in terms of the parameters to be optimized by applying the logarithmic operator:

$$\log|S(f,z)| = \log|P(f)| + \log|G| - 2\alpha(f)z$$

G is a constant which absorbs the backscatter coefficient B_0 and the original gain factor G'.

For soft tissues, the attenuation is often assumed proportional to frequency, that is, $\alpha(f) = \alpha f$. However, the behavior of microbubbles in an ultrasound field is more complex and leads to a resonance peak in the MHz frequency range.[58] Therefore, the frequency-dependent attenuation coefficient of PVA-PFB microbubbles entrapped in polyacrylamide was determined using the reference phantom method.[55,59,60] This demonstrated that beyond resonance and within the bandwidth of the ultrasound probe [3–9 MHz, see Fig. 3(b)], the attenuation coefficient could be approximated by a linear decrease with frequency, that is:

$$\alpha(f) = a - bf.$$

Substitution of the latter in the linearized equation resulted in a linear least squares optimization problem, which can be simultaneously solved for G, a, and b using a single-shot solver.[53]

The peak attenuation $\alpha_p = a - bf_{res}$ was chosen as an estimation of the true bubble density profile as an increase in microbubble density results in a higher resonance peak [Fig. 3(b)]. The measured backscattered spectrum was

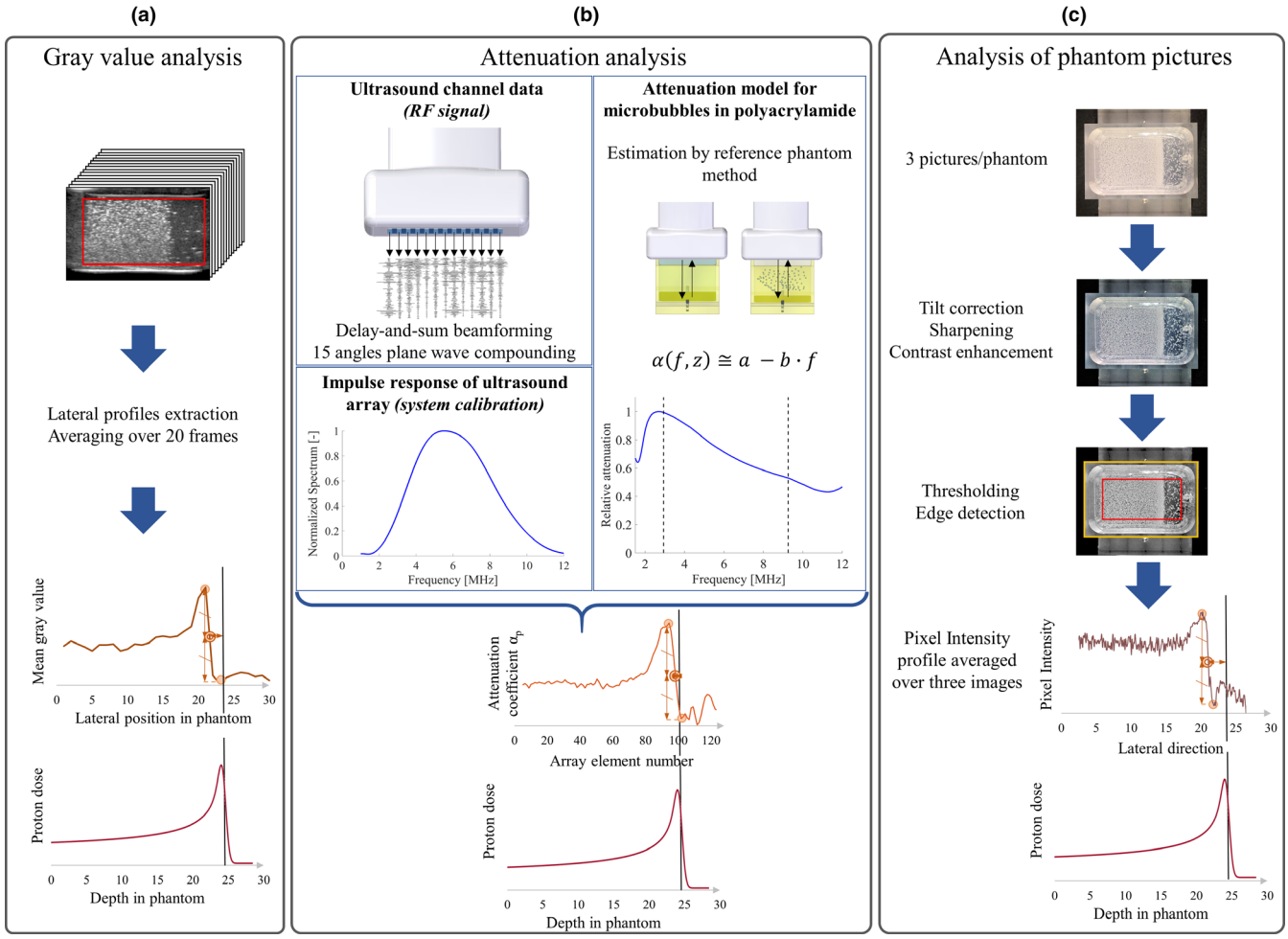

FIG. 3. Image processing workflow for three different types of analysis based on (a) the ultrasound gray value, (b) the ultrasound attenuation coefficient, and (c) pictures of the phantoms (for 50°C phantoms, 10 Gy). For all three methods, vaporization profiles as a function of the distance traveled by the proton beam were extracted, and related to the proton depth-dose profile and the proton range. The displayed gray value, attenuation, and pixel intensity profile schematics do not represent experimental data and are for illustrative purposes. [Color figure can be viewed at wileyonlinelibrary.com]

obtained after having applied coherent beamforming (delay-and-sum followed by plane wave compounding[61]) to the radiofrequency (RF) channel data, and averaged in the frequency domain over the 20 ultrasound frames. Lateral profiles of α_p, parallel to the proton beam, were obtained by solving the optimization problem for 128 positions (corresponding to the center of individual transducer array elements) and the 50% drop in the attenuation profile was determined and compared to the proton range in the same way as for the gray value profiles (see Section 2.E.1).

2.E.3. Analysis of phantom pictures

As an independent method (with respect to the aforementioned ultrasound-based analyses) to locate the distal edge of the microbubble contrast zone, pixel intensity profiles were derived from phantom pictures as depicted in Fig. 3(c). First, tilts in the image plane were removed and the contrast and sharpness were enhanced. Then, images were processed in Matlab (R2019a, MathWorks, NA, USA) and the outer edges of the phantom container were delineated using thresholding followed by edge detection, in order to derive a pixel-to-mm conversion factor based on the known phantom length. Afterwards, an ROI was defined within the polyacrylamide gel, and pixel intensity profiles across the lateral direction were extracted by averaging intensity values along the phantom width. The individual profiles of the three images per phantom were averaged. Finally, the position of the 50% drop in pixel intensity was determined as described earlier (Section 2.E.1) and compared with the proton range. The photographic analysis was intended as a semiquantitative analysis, as the pixel intensity was not expected to be linearly related to the microbubble concentration. However, the sharp drop in bubble concentration could be accurately located on the images and compared to the proton range.

3. RESULTS

3.A. Radiation response at physiological temperature

Ultrasound images of polyacrylamide phantoms with dispersed PCDA-PFB and PVA-PFB nanodroplets heated to 37°C prior to irradiation are presented in Fig. 4, and show

that a substantial fraction of PCDA-PFB nanodroplets already vaporizes at 37°C before irradiation [Fig. 4(b)]. Due to the large background signal in ultrasound images of PCDA-PFB phantoms, no difference in contrast could be observed between zones proximal and distal to the proton range after irradiation. This lack of thermal stability explains the necessity to shift to PVA-PFB droplets in these experiments at elevated degrees of superheat. Indeed, Fig. 4(a) demonstrates the superior stability of PVA-PFB droplets at temperatures well above the PFB boiling point (−2°C), resulting in a limited background signal. For PVA-PFB phantoms, a strong increase in contrast was observed proximal to the proton range after irradiation, as shown in Fig. 5(a). Gray value profiles are displayed in Fig. 5(b) for the six irradiated PVA-PFB phantoms and the three control phantoms, together with the proton depth-dose deposition profile. The gray value profiles indicate a rather uniform bubble density, dropping close to the proton range. The signal shift, calculated as the difference between the proton range (R_{80}) and the position of the 50% drop in ultrasound gray value, was 0.17 mm ± 0.20 mm.

3.B. Primary proton sensitization (50°C)

Ultrasound images of phantoms with dispersed PVA-PFB nanodroplets, heated to 50°C, are displayed in Fig. 6 before (a) and after proton irradiation with a dose of 10 Gy (b). The small number of background microbubbles before irradiation [Fig. 6(a)] confirms the thermal stability of PVA-PFB nanodroplets for high degrees of superheat. For irradiated phantoms, a contrast increase was observed in the proton path, with an additional enhancement around the Bragg peak location [Fig. 6(b)], which was also observed visually [Fig. 6(c)]. The strength of the induced contrast resulted in acoustic shadowing, particularly in the Bragg peak region. Hence, only the upper rectangular ROI, bounded by the red line [Fig. 6(b)], was used to derive the gray value profiles. For the estimation of the attenuation parameter, the complete ROI was employed [magenta rectangle in Fig. 6(b)]. Three different profiles were derived from ultrasound and optical images, as described in Section 2.E, in order to estimate the microbubble density along the proton path and compare the end of the vaporized zone with the proton range. The profiles are displayed in Figs. 6(d)–6(f) together with the Bragg curve and the proton range. Qualitatively, all three analysis methods yield similar vaporization profiles, with an increase around the location of the Bragg peak and a sharp drop distal to the proton distal dose fall-off. The ratio between the vaporization profiles proximal to the Bragg peak (in the plateau region) and the peak value is higher than the measured skin-to-peak dose ratio of the protons (0.2). Ultrasound attenuation and gray value profiles agree with each other with similar peak-to-plateau ratios, although the ROIs used for the two techniques differ. This demonstrates that the ultrasound attenuation analysis is not adversely impacted by acoustic

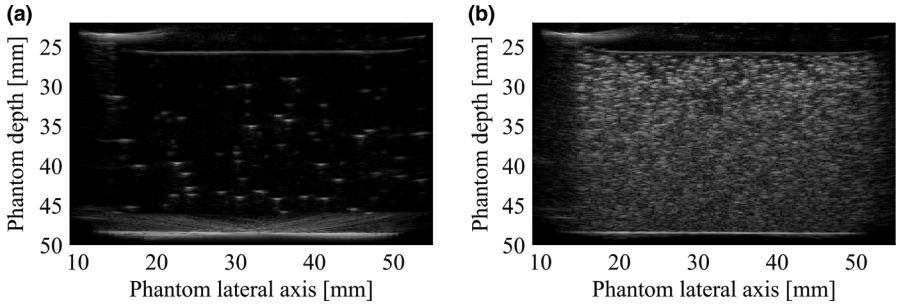

FIG. 4. Ultrasound images of polyacrylamide gels with (a) dispersed PVA-PFB nanodroplets or (b) PCDA-PFB nanodroplets, after heating to 37°C through immersion in a warm water bath (no irradiation).

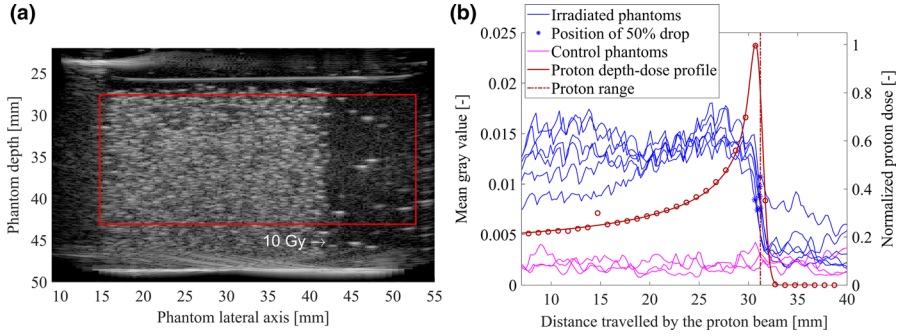

FIG. 5. (a) Ultrasound image of a polyacrylamide gel phantom with dispersed PVA-PFB nanodroplets, after irradiation by a 62 MeV proton beam (10 Gy dose) at 37°C. The red rectangle (online version only) is the region of interest used to derive gray value profiles. (b) Gray value profiles for six irradiated and three control PVA-PFB phantoms along the lateral axis of the ultrasound image, with the proton Bragg curve and range position superimposed. The position of the 50% drop in mean gray value is indicated by a star on each profile post-irradiation. [Color figure can be viewed at wileyonlinelibrary.com]

shadowing, as a full ROI could be employed. For all phantoms, the width of the zone with higher bubble density at the end of the proton range appeared larger than the Bragg peak width. The signal shifts between the proton R_{80} value and the 50% drops in gray value or α_p were −0.74 mm ± 0.09 mm and −0.86 mm ± 0.04 mm, respectively. As an independent evaluation of the relationship between the proton range and the microbubble generation, signal shifts were also derived from phantom pictures and yielded a value of −0.64 mm ± 0.29 mm.

Finally, an ultrasound image of the phantom irradiated with a clinical dose of 2 Gy is displayed in Fig. 7, together with the corresponding gray value and attenuation profiles. Although less pronounced compared to 10 Gy irradiations, acoustic shadowing is also observed in the Bragg peak vicinity, where the largest microbubble density was found. The signal shifts were – 0.52 mm for the gray value profile, and – 0.78 mm for the attenuation profile. The peak-to-plateau ratios were higher than for the 10 Gy case, both for the gray value and attenuation profile. The fact that the contrast peak-to-plateau ratio displayed in Fig. 7 is very similar to the peak-to-plateau ratio of the proton dose deposition profile is coincidental, as the microbubble density is not expected to follow the depth-dose deposition profile, but should rather depend on the fluence of the different particles that can trigger vaporization (primary protons and secondaries) and their local LET.

4. DISCUSSION

For both temperatures, a noticeable increase in ultrasound contrast was observed after irradiation with 62 MeV protons, confirming the potential of superheated injectable nanodroplets for *in vivo* proton range verification. Comparison between PCDA-PFB and PVA-PFB nanodroplets highlighted the critical role of the encapsulating shell to stabilize the nanodroplets at elevated temperatures, well above the superheated liquid boiling point.

4.A. Influence of the temperature on the ultrasound contrast generation

The average ultrasound gray value in the plateau region (and peak region at 50°C) is shown in Fig. 8(a) for the tested

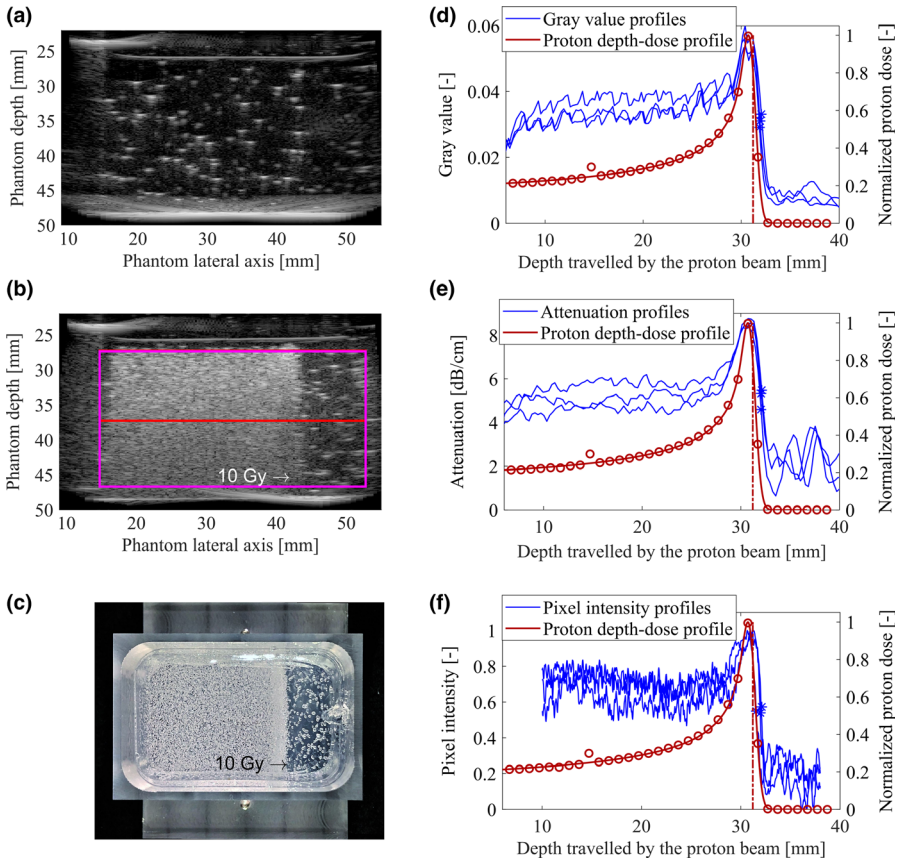

FIG. 6. Ultrasound images of PVA-PFB nanodroplets dispersed in polyacrylamide hydrogel phantoms and heated to 50°C, (a) before irradiation, and (b) after proton irradiation with a dose of 10 Gy. The region of interest (ROI) used for ultrasound gray value analysis is displayed in red, and the ROI for attenuation analysis is shown in magenta (online version only). (c) Picture of an irradiated phantom. (d) Gray value and (e) attenuation profiles were derived from the ultrasound images, and the position of the 50% distal profile drop was identified (stars). Additionally, phantom pictures were analyzed to extract pixel intensity profiles (f) and corresponding 50% drop (stars). The proton depth-dose deposition profile is displayed in red (online version only), and the proton range (R_{80}) is the vertical dashed line. [Color figure can be viewed at wileyonlinelibrary.com]

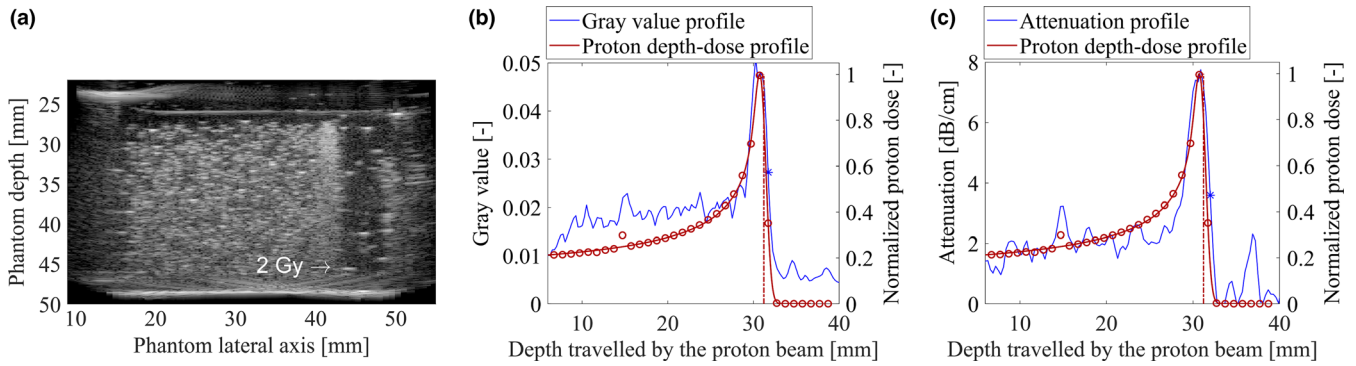

FIG. 7. (a) Ultrasound image of a polyacrylamide phantom with dispersed PVA-PFB nanodroplets after irradiation with 62 MeV protons (dose of 2 Gy) at 50°C. (b) Gray value and (c) attenuation profiles derived from the ultrasound images, with the Bragg curve superimposed (in red, online version only) and a vertical line representing the proton range. The stars indicate the 50% distal drop position of the ultrasound-based profiles. [Color figure can be viewed at wileyonlinelibrary.com]

temperatures and compared to our earlier findings at 25°C,[25] demonstrating an increase in the generated ultrasound contrast with temperature. The radiation-induced nucleation theory[26] predicts a temperature-dependent LET threshold given by:

$$\left\langle \frac{dE}{dx} \right\rangle_{L_{eff}} \geq \frac{W_{tot}}{kR_c}$$

where W_{tot} is the total energy required to nucleate a critical embryo of radius R_c in the superheated liquid, and the effective length is given as $L_{eff} = kR_c$. The semiempirical nucleation parameter k is assumed to be equal to 2, a reasonable assumption for nucleation energies well below 1 MeV[31] (e.g., W_{tot} is 13 keV at 37°C). Both at 25°C and 37°C, the LET thresholds (370 and 145 keV/μm, respectively) are above the maximum LET reached by protons or secondary electrons. Therefore, nucleation is expected to be induced by heavy recoil nuclei generated by nonelastic interactions of protons with the phantom matrix or the nanodroplets themselves, as well as by similarly released alpha particles, whose LET lie in the range 130–190 keV/μm,[62] for the 37°C case. At 50°C, the predicted threshold drops further down to 60 keV/μm, allowing sensitization to primary protons that reach an LET up to 70–90 keV/μm at the very end of their range,[63] while being too high to observe vaporization induced by secondary electrons (LET of 25–30 keV/μm[31]). This sensitization to the primary proton beam is clearly demonstrated by the strong contrast increase at the end of the vaporization curves and could even be observed visually (Figs. 6 and 7).

The contrast increase with temperature in the plateau region can thus be explained by the decrease in the LET threshold with temperature, making nanodroplets sensitive to a broader range of charged particles. Furthermore, the higher the temperature, the longer the track length over which charged particles have a sufficient LET to induce nanodroplet vaporization, and consequently the higher the likelihood of vaporization. In contrast to the 25°C and 37°C case, a strong increase in gray value was observed at the end of the proton range at 50°C. As shown in Fig. 8(a), the contrast difference between the plateau region and the peak ultrasound contrast is rather small compared to the fluence ratio between primary protons and secondary particles (as only 1% of the primary protons undergo nonelastic nuclear interactions per cm[64]), which would predict a stronger contrast increase upon proton sensitization. The relatively low contrast increase observed at the end of the proton range could be attributed to the imaging modality, as the microbubble concentration was high enough to induce signal saturation and acoustic shadowing. Moreover, the large microbubble density observed in the peak might have caused a drop of the local nanodroplet concentration over the course of the irradiation, leading to a progressive decrease in the probability of a proton-droplet interaction. These hypotheses are further supported by the lack of proportionality observed between the peak contrast and the proton peak dose, as shown by the 2 and 10 Gy bars of Fig. 8(a).

4.B. Influence of the temperature on the relationship between the proton range and the ultrasound contrast

Both at 37°C and 50°C, a reproducible relationship was obtained between the proton depth-dose deposition profile and the generated ultrasound contrast, as evidenced by the submillimeter reproducible shift between the 50% signal drop and the proton R_{80} value. Interestingly, despite small (<0.3 mm) variations on the exact signal shift, a high reproducibility of the signal curves at 50°C was achieved, irrespective of the applied analysis method. Comparing the profiles at 37°C and 50°C with our earlier findings at 25°C [Fig. 8(b)], one can notice that the drop in ultrasound contrast shifts deeper into the phantom with increased degree of superheat. This is also caused by the drop in LET threshold with temperature. Indeed, at 25°C, the energy of the primary protons in the final few millimeters of their range was too low to produce recoil nuclei with sufficient LET to trigger vaporization events.[25] At 37°C, most secondary particles will have a sufficient LET, and the signal generation is expected to be solely dependent on the occurrence of nuclear reactions. Hence, the proton beam needs to have enough energy to exceed the Coulomb barrier. The most important elements in the phantom are C,

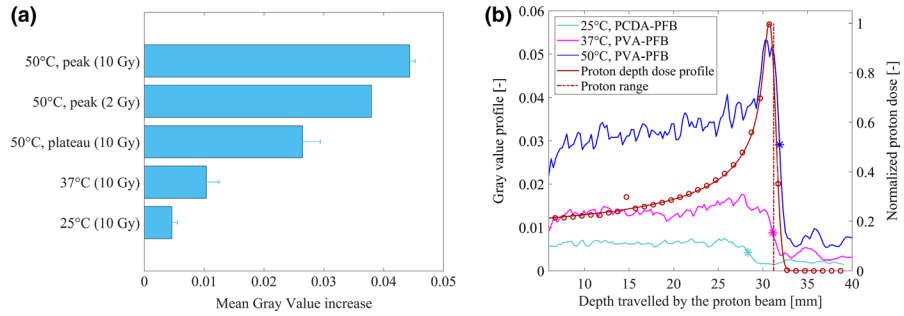

FIG. 8. (a) Gray value increase observed on ultrasound images due to nanodroplet vaporization at different temperatures. The 25°C data correspond to a previous study with PCDA-PFB nanodroplets. Error bars correspond to the standard deviation in gray value increase, for available phantoms at each temperature (b) Ultrasound gray value profiles for three temperatures were superimposed on a Bragg curve. The 50% drop in contrast position is indicated by a star. [Color figure can be viewed at wileyonlinelibrary.com]

N, O, and F (apart from H), with approximate Coulomb barriers between 3 and 5 MeV.[65] The corresponding residual proton range explains why the ultrasound contrast drops earlier than in the 50°C case, where the primary proton sensitization ensures contrast generation until the very end of their range. Both at 25°C and 37°C, the shape of vaporization profiles is dictated by the production cross-sections of relevant secondary particles as well as their likelihood to traverse a droplet while having a sufficient LET.

At 50°C, the end of the vaporization profile is expected to coincide with the end of the proton range. Due to the energy dispersion of the proton source combined with range straggling, the range spread was modeled as a Gaussian with a sigma value of 0.54 mm (based on the analytical fit of the measured proton depth-dose deposition). Figure 9 overlays ultrasound gray value profiles after irradiation (doses of 2 and 10 Gy) with the estimated proton stopping distribution, indicating that the ultrasound contrast profile is broader and peaks slightly earlier than expected. Indeed, the contrast profile was expected to peak at the R_{80} position, where the density of stopping protons is the highest (dotted curve). The broadening of the peak could be attributed to the potential ultrasound contrast saturation, which results in the true contrast peak being cropped, and by the fact that the gray value profiles are modulated by the point spread function (PSF) of the ultrasound system (0.63 mm FWHM). These also contribute to the negative signal shift of $-0.74\ \text{mm} \pm 0.09\ \text{mm}$. The slight offset (<1 mm) between the contrast peak and the proton range is believed to arise from measurement uncertainties elaborated later. While for lower temperatures the signal shift between the 50% drop and R_{80} value was preferred (maximal slope at 50% drop makes this characteristic value more robust to fluctuations on the profile), the 50% drop is less relevant when proton sensitization occurs. A more interesting relationship would in this case be between the ultrasound signal peak and the proton range, as these are expected to be aligned. However, due to a presumed saturation of the signal, we opted not to do so here.

4.C. Implications, limitations, and future directions

In this study, the radiation-induced vaporization of superheated, injectable nanodroplets was validated at physiological temperature. As shown in Fig. 4, it was crucial to ensure the stability of the nanodroplet formulation at increased temperatures. While PCDA-PFB droplets were unsuitable, PVA-PFB droplets showed promising thermal stability *in vitro*. This also demonstrates the robustness of the concept to different chemical formulations. Indeed, while we expect that the shell viscoelastic properties and surface tension have an influence on the LET threshold for vaporization (the influence of the surrounding polyacrylamide matrix was found to be negligible), the latter is mainly defined by the superheated core liquid. This knowledge, in combination with the versatility of nanoplatforms under development in different fields of biomedical research, allows the further development of these or similar particles toward an *in vivo* application where additional modifications of the shell (e.g., pegylation) might be required to secure biocompatibility and reasonable circulatory lifetimes.[66] Moreover, functionalization of the shell with targeting ligands (e.g., antibodies, peptides, etc.) could achieve nanodroplet accumulation inside the tumor volume, ensuring signal generation at the location of primary interest

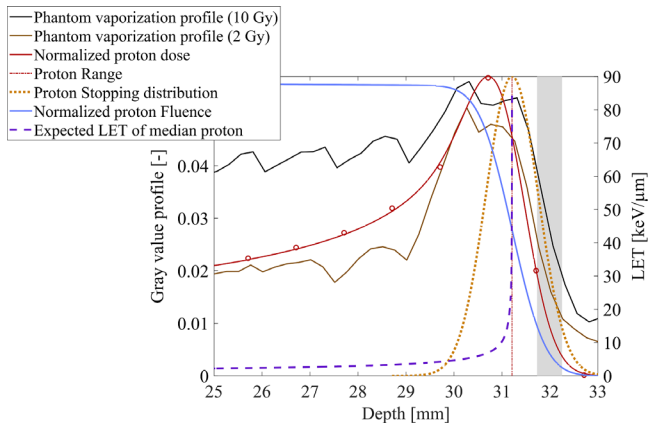

FIG. 9. Representative gray value profiles at 50°C (2 and 10 Gy) superimposed on the proton depth-dose deposition profile, proton fluence, and Gaussian distribution of proton stopping positions. The shaded area represents the confidence interval on the position of the 50% drop in ultrasound gray value (extracted from the three phantoms which received a dose of 10 Gy). The linear energy transfer (LET) of a proton stopping at the R_{80} position is also illustrated (dashed curve). [Color figure can be viewed at wileyonlinelibrary.com]

and possibly counteracting biological wash-out. However, potential particle detachment due to vaporization remains to be assessed. On the long term, we can even envision targeted, radiation-induced release of chemotherapeutics by upgrading these functionalized contrast agents toward drug delivery vehicles.[67] On a shorter term, also nontargeted droplets could serve *in vivo* applications either in combination with online imaging, visualizing vaporization events in real time, or for proton therapy of liver tumors, as particles of this size are expected to spontaneously accumulate in the liver (clearance by the reticulo-endothelial system[67]).

The strong ultrasound contrast resulting from the phase transition of nanodroplets into echogenic microbubbles enables the extraction of vaporization profiles whose sharp fall-off could be related to the proton range with submillimeter accuracy, both through gray value analysis and attenuation estimation. This was confirmed independently, for the 50°C phantoms, by optical images. Uncertainties in the alignment of vaporization profiles with the proton depth-dose profile were estimated to be 0.22 mm (the standard deviation of the alignment fiducials' lateral ultrasound coordinate used for image registration, see Fig. 2) for ultrasound-based analysis (gray value and attenuation), and 0.36 mm (the interphantom standard deviation of the phantom container length retrieved from the images) for optical images. Additionally, as microbubbles could not be counted individually due to the large bubble densities, the image resolution was limited by diffraction[68] and the microbubble localization accuracy was characterized by the lateral Gaussian PSF of the ultrasound system (0.63 mm). Moreover, the reported signal shifts also rely on the accuracy of the absolute R_{80} value, which suffers from uncertainty ($\pm$0.5 mm) related to the limited resolution of the diode and Gafchromic film measurements, as well as TRIM simulation accuracies. Overall, the three evaluation methods (gray value, attenuation, optical) agreed on the level of the respective image resolution, cross-validating each other. However, this submillimeter accuracy was reported in idealized *in vitro* conditions. The signal shift retrieval performance remains to be determined in physiological conditions, with heterogeneous tissue densities, and might be influenced by different factors such as inhomogeneities in nanodroplet distribution, speed of sound mismatch, multiple scattering or acoustic shadowing. While attenuation estimation could help reduce the effects of acoustic shadowing by dense microbubble populations, online high frame rate imaging (up to thousands of frames per second) could be beneficial to minimize the impact of ultrasound contrast saturation or multiple scattering, for instance. Besides, online ultrasound imaging (either active or passive, relying on the detection of individual acoustic signals emitted during phase change[69]) enables real-time feedback over the course of the irradiation, and could greatly improve the microbubble localization accuracy through super-resolution ultrasound imaging.[70] While targeted microbubbles could potentially be imaged offline a few minutes post-irradiation (expecting their *in vivo* lifetime to be sufficient[71]), online high frame rate imaging would allow to perform range verification both for targeted or nonfunctionalized, freely flowing contrast agents, by means of differential imaging and microbubble tracking.[70]

Similarly to PET and prompt gamma imaging, at 37°C, the radiation-induced nanodroplet response is expected to rely solely on nuclear reaction products, only indirectly visualizing the proton irradiation. While the vaporization profiles could qualitatively be explained by means of the radiation-induced nucleation theory, comprehensive Monte Carlo simulations should be the next step toward a full understanding of the relationship between different features of the vaporization profiles and the proton range. Moreover, nanodroplet vaporization was evaluated in a mono-energetic, broad proton beam, and should be assessed for clinically relevant treatment plans, where the ultrasound contrast relationship to the proton range is expected to become more complex. The contrast generation was evaluated for a limited range of doses (2 and 10 Gy) and the minimum dose for which the proton range can be accurately detected remains to be determined. The impact of the generated gaseous microbubbles on the proton treatment delivery was estimated to be negligible (shift in range well below 1 mm) for clinically relevant doses. In comparison with other range verification techniques currently under investigation, ultrasound-based detection of nanodroplet vaporization for range verification would be particularly suitable for treatment sites of sonic accessibility, such as the prostate, breast or liver, where tissue motion and anatomical changes tend to lead to large range uncertainties.[5,72] The advantage of using ultrasound for conventional imaging would be that it enables direct coregistration of the proton range with tissue anatomy.[19,73]

Interestingly, at 50°C, we demonstrated that a sufficient degree of superheat sensitizes the superheated core to protons, motivating further exploration of this technique for application to proton dosimetry. Nevertheless, achieving such a degree of superheat at body temperature would require additional modifications of the nanodroplet design. One possibility would be to change the core to a lower-boiling point liquid, for example, octafluoropropane (b.p. = −37°C). However, the reduced stability makes these droplets difficult to handle.[74] Recently, endoskeletal droplets with highly tunable vaporization properties were introduced,[75] potentially bringing direct *in vivo* proton detection and range verification within reach.

5. CONCLUSION

The ultrasound contrast generation from phase-change nanodroplets after proton irradiation at 37°C and 50°C was evaluated in tissue-mimicking phantoms. This elucidated the importance of the nanodroplet design to ensure stability at elevated temperatures and demonstrated the feasibility of the concept for a different nanodroplet formulation. Our recent proof-of-concept study, which showed radiation-induced vaporization of superheated nanodroplets in proton beams at 25°C, was extended to a physiological temperature, taking the next step toward an *in vivo* application. Raising the temperature further to 50°C led to a strong contrast increase at the Bragg peak location attributed to the vaporization of the

nanodroplets by primary protons at the end of their range. Comparison of the radiation-induced contrast generation at different temperatures showed that the overall contrast increases with increasing degree of superheat and that the contrast profiles shift closer toward the proton range. This was explained by the radiation-induced nucleation theory, as the LET threshold decreases with temperature, resulting in vaporization by heavy recoil nuclei only at 25°C, lighter nuclei such as alpha particles at 37°C, and proton detection at 50°C. The positions of the 50% drop in contrast were retrieved from ultrasound images (at 37°C and 50°C) and optical images (50°C) and were related to the proton range with submillimeter reproducibility. Overall, these findings further confirm the potential and tunability of injectable phase-change nanodroplets as a proton range verification technique in an indirect (through secondary reaction products) mode and unveil the possibility of reaching direct range verification through detection of primary protons.

ACKNOWLEDGMENTS

The authors thank the "Centre de Ressources du Cyclotron" of UCLouvain for the irradiation experiments, absolute range measurements, and fruitful discussion. The authors also thank Fraunhofer IBMT for lending the DiPhAs ultrasound scanner, and the mechanical and electrical staff of the Physics Department of KU Leuven for manufacturing phantom containers as well as the water tank with temperature control. This work has been supported by the European Union's Horizon 2020 research and innovation programme under grant agreement n°766456 ("AMPHORA"). BC received a PhD fellowship fundamental research from the Research Foundation Flanders (n°11A9520N).

CONFLICT OF INTEREST

The authors have no relevant conflict of interest to disclose.

DATA AVAILABILITY STATEMENT

The data that support the findings of this study are available from the corresponding author upon reasonable request.

*Sophie V. Heymans and Bram Carlier should be considered joint first author.
†Edmond Sterpin and Koen Van Den Abeele should be considered joint last author.
a)Author to whom correspondence should be addressed. Electronic mail: .

REFERENCES

1. Thariat J, Hannoun-Levi JM, Sun Myint A, Vuong T, Gérard JP. Past, present, and future of radiotherapy for the benefit of patients. *Nat Rev Clin Oncol*. 2013;10:52–60.
2. Knopf AC, Lomax A. In vivo proton range verification: a review. *Phys Med Biol*. 2013;58:R131.
3. Moteabbed M, España S, Paganetti H. Monte Carlo patient study on the comparison of prompt gamma and PET imaging for range verification in proton therapy. *Phys Med Biol*. 2011;56:1063–1082.
4. Paganetti H. Range uncertainties in proton therapy and the role of Monte Carlo simulations. *Phys Med Biol*. 2012;57:R99.
5. Polf JC, Parodi K. Imaging particle beams for cancer treatment. *Phys Today*. 2015;68:28–33.
6. Parodi K, Enghardt W. Potential application of PET in quality assurance of proton therapy. *Phys Med Biol*. 2000;45:N151.
7. Parodi K, Paganetti H, Shih HA, et al. Patient study of in vivo verification of beam delivery and range, using Positron Emission Tomography and Computed Tomography Imaging after proton therapy. *Int J Radiat Oncol Biol Phys*. 2007;68:920–934.
8. Min CH, Zhu X, Winey BA, et al. Clinical Application of in-room PET for in vivo treatment monitoring in proton radiotherapy. *Int J Radiat Oncol Biol Phys*. 2013;86:183–189.
9. Helmbrecht S, Santiago A, Enghardt W, Kuess P, Fiedler F. On the feasibility of automatic detection of range deviations from in-beam PET data. *Phys Med Biol*. 2012;57:1387–1397.
10. España S, Zhu X, Daartz J, et al. The reliability of proton-nuclear interaction cross-section data to predict proton-induced PET images in proton therapy. *Phys Med Biol*. 2011;56:2687–2698.
11. Stichelbaut F, Jongen Y. Verification of the proton beams position in the patient by the detection of prompt gamma-rays emission. In: *39th Meeting of the Particle Therapy Co-Operative Group*. Presented at the PTCOG 39, San Francisco; 2003.
12. Xie Y, Bentefour EH, Janssens G, et al. Prompt gamma imaging for in vivo range verification of pencil beam scanning proton therapy. *Int J Radiat Oncol Biol Phys*. 2017;99:210–218.
13. Smeets J, Roellinghoff F, Prieels D, et al. Prompt gamma imaging with a slit camera for real- time range control in proton therapy. *Phys Med Biol*. 2012;57:3371–3405.
14. Rohling H, Priegnitz M, Schoene S, et al. Requirements for a Compton camera for in vivo range verification of proton therapy. *Phys Med Biol*. 2017;62:2795.
15. Jones KC, Nie W, Chu JCH, et al. Acoustic-based proton range verification in heterogeneous tissue: simulation studies. *Phys Med Biol*. 2018;63:025018.
16. Jones KC, Vander Stappen F, Bawiec CR, et al. Experimental observation of acoustic emissions generated by a pulsed proton beam from a hospital-based clinical cyclotron. *Med Phys*. 2015;42:7090–7097.
17. Patch SK, Kireeff Covo M, Jackson A, et al. Thermoacoustic range verification using a clinical ultrasound array provides perfectly co-registered overlay of the Bragg peak onto an ultrasound image. *Phys Med Biol*. 2016;61:5621–5638.
18. Kellnberger S, Assmann W, Lehrack S, et al. Ionoacoustic tomography of the proton Bragg peak in combination with ultrasound and optoacoustic imaging. *Sci Rep*. 2016;6:29305.
19. Hickling S, Xiang L, Jones KC, et al. Ionizing radiation-induced acoustics for radiotherapy and diagnostic radiology applications. *Med Phys*. 2018;45:e707–e721.
20. Patch SK, Hoff DEM, Webb TB, Sobotka LG, Zhao T. Two-stage ionoacoustic range verification leveraging Monte Carlo and acoustic simulations to stably account for tissue inhomogeneity and accelerator-specific time structure - A simulation study. *Med Phys*. 2018;45:783–793.
21. Lehrack S, Assmann W, Bertrand D, et al. Submillimeter ionoacoustic range determination for protons in water at a clinical synchrocyclotron. *Phys Med Biol*. 2017;62:L20–L30.
22. Gensheimer MF, Yock TI, Liebsch NJ, et al. In vivo proton beam range verification using spine MRI changes. *Int J Radiat Oncol Biol Phys*. 2010;78:268–275.
23. Yuan Y, Andronesi OC, Bortfeld TR, et al. Feasibility study of in vivo MRI based dosimetric verification of proton end-of-range for liver cancer patients. *Radiother Oncol*. 2013;106:378–382.
24. Parodi K, Polf JC. In vivo range verification in particle therapy. *Med Phys*. 2018;45:e1036–e1050.
25. Carlier B, Heymans SV, Nooijens S, et al. Proton range verification with ultrasound imaging using injectable radiation sensitive nanodroplets: a feasibility study. *Phys Med Biol*. 2020;65:065013.

26. D'Errico F. Radiation dosimetry and spectrometry with superheated emulsions. *Nucl Instruments Methods Phys Res Sect B Beam Interact with Mater Atoms*. 2001;184:229–254.
27. Apfel RE. The superheated drop detector. *Nucl Instruments Methods*. 1979;162:603–608.
28. Mountford PA, Borden MA. On the thermodynamics and kinetics of superheated fluorocarbon phase-change agents. *Adv Colloid Interface Sci*. 2016;237:15–27.
29. Seitz F. On the theory of the bubble chamber. *Phys Fluids*. 1958;1:2–13.
30. West CD. *Cavitation Bubble Nucleation by Energetic Particles*. Oak Ridge, Tenessee: Oak Ridge National Laboratory; 1998.
31. D'Errico F. Fundamental properties of superheated drop (bubble) detectors. *Radiat Prot Dosimetry*. 1999;84:55–62.
32. Sarkar R, Chatterjee BK, Roy B, Roy SC. Radiation detection by using superheated droplets. *Radiat Phys Chem*. 2006;75:2186–2194.
33. Roy SC. Superheated liquid and its place in radiation physics. *Radiat Phys Chem*. 2001;61:271–281.
34. Felizardo M, Morlat T, Marques JG, et al. Fabrication and response of high concentration SIMPLE superheated droplet detectors with different liquids. *Astropart Phys*. 2013;49:28–43.
35. Miller A, Machrafi R, Benton E, Kitamura H, Kodaira S. Comparison of the space bubble detector response to space-like neutron spectra and high energy protons. *Acta Astronaut*. 2018;151:1–6.
36. d'Errico F. Status of radiation detection with superheated emulsions. *Radiat Prot Dosimetry*. 2006;120:475–479.
37. D'Errico F, Nath R, Lamba M, Holland SK. A position-sensitive superheated emulsion chamber for three-dimensional photon dosimetry. *Phys Med Biol*. 1998;43:1147–1158.
38. Apfel RE. Activatable infusable dispersions containing drops of a superheated liquid for methods of therapy and diagnosis. 1998;(US Patent 5,840,276).
39. Sheeran PS, Dayton PA. Phase-change contrast agents for imaging and therapy. *Curr Pharm Des*. 2012;18:2152–2165.
40. Sheeran PS, Matsuura N, Borden MA, et al. Methods of generating submicrometer phase-shift perfluorocarbon droplets for applications in medical ultrasonography. *IEEE Trans Ultrason Ferroelectr Freq Control*. 2016;64:252–263.
41. Lea-Banks H, O'Reilly MA, Hynynen K. Ultrasound-responsive droplets for therapy: a review. *J Control Release*. 2019;293:144–154.
42. Reznik N, Williams R, Burns PN. Investigation of vaporized submicron perfluorocarbon droplets as an ultrasound contrast agent. *Ultrasound Med Biol*. 2011;37:1271–1279.
43. Sheeran PS, Luois SH, Mullin LB, Matsunaga TO, Dayton PA. Design of ultrasonically-activatable nanoparticles using low boiling point perfluorocarbons. *Biomaterials*. 2012;33:3262–3269.
44. Toumia Y, Cerroni B, Domenici F, et al. Phase change ultrasound contrast agents with a photopolymerized diacetylene shell. *Langmuir*. 2019;35:10116–10127.
45. Dove JD, Mountford PA, Murray TW, Borden MA. Engineering optically triggered droplets for photoacoustic imaging and therapy. *Biomed Opt Express*. 2014;5:4417.
46. Bortfeld T. An analytical approximation of the Bragg curve for therapeutic proton beams. *Med Phys*. 1997;24:2024–2033.
47. Ziegler JF. SRIM-2013 software package. http://www.srim.org. Published 2013. Accessed June 17, 2020.
48. Crijns W, Maes F, Van Der Heide UA, Van Den Heuvel F. Calibrating page sized Gafchromic EBT3 films. *Med Phys*. 2013;40:012102.
49. Fiorini F, Kirby D, Thompson J, et al. Under-response correction for EBT3 films in the presence of proton spread out Bragg peaks. *Phys Medica*. 2014;30:454–461.
50. Soetanto K, Chan M. Fundamental studies on contrast images from different-sized microbubbles: analytical and experimental studies. *Ultrasound Med Biol*. 2000;26:81–91.
51. Klibanov AL. Targeted delivery of gas-filled microspheres, contrast agents for ultrasound imaging. *Adv Drug Deliv Rev*. 1999;37:139–157.
52. Marsh JN, Hughes MS, Hall CS, et al. Frequency and concentration dependence of the backscatter coefficient of the ultrasound contrast agent Albunex®. *J Acoust Soc Am*. 1998;104:1654–1666.
53. Muraleedharan A, Bertrand A, D'hooge J. A linear least squares based estimation of spatial variation of the attenuation coefficient from ultrasound backscatter signals. In: Proceedings of Meetings on Acoustics ICU. Vol 38. Acoustical Society of America; 2019:020016. https://doi.org/10.1121/2.0001266.
54. Kruizinga P, Mastik F, De Jong N, van der Steen AFW, Van Soest G. Plane-wave ultrasound beamforming using a nonuniform fast fourier transform. *IEEE Trans Ultrason Ferroelectr Freq Control*. 2012;59:2684–2691.
55. Segers T, de Jong N, Versluis M. Uniform scattering and attenuation of acoustically sorted ultrasound contrast agents: modeling and experiments. *J Acoust Soc Am*. 2016;140:2506–2517.
56. de Jong N, Emmer M, van Wamel A, Versluis M. Ultrasonic characterization of ultrasound contrast agents. *Med Biol Eng Comput*. 2009;47:861–873.
57. de Jong N, Hoff L. Ultrasound scattering properties of Albunex microspheres. *Ultrasonics*. 1993;31:175–181.
58. Leighton TG. *The Acoustic Bubble*. San Diego, CA, USA: Academic Press Inc.; 1994.
59. Hoff L, Sontum PC, Hovem JM. Oscillations of polymeric microbubbles: Effect of the encapsulating shell. *J Acoust Soc Am*. 2000;107:2272–2280.
60. Raymond JL, Haworth KJ, Bader KB, et al. Broadband attenuation measurements of phospholipid-shelled ultrasound contrast agents. *Ultrasound Med Biol*. 2014;40:410–421.
61. Montaldo G, Tanter M, Bercoff J, Benech N, Fink M. Coherent plane-wave compounding for very high frame rate ultrasonography and transient elastography. *IEEE Trans Ultrason Ferroelectr Freq Control*. 2009;56:489–506.
62. Grassberger C, Paganetti H. Elevated LET components in clinical proton beams. *Phys Med Biol*. 2011;56:6677–6691.
63. Green AR, Andrews HR, Bennett L, et al. Bubble detector characterization for space radiation. *Acta Astronaut*. 2005;56:949–960.
64. Durante M, Paganetti H. Nuclear physics in particle therapy: a review. *Reports Prog Phys*. 2016;79:096702.
65. Haji-Saeid M, Mra P, Ruth T, et al. Cyclotron Produced Radionucleids: Physical Characteristics and Production Methods. 2009.
66. Jokerst JV, Lobovkina T, Zare RN, Gambhir SS. Nanoparticle PEGylation for imaging and therapy. *Nanomedicine*. 2011;6:715–728.
67. Cao Y, Chen Y, Yu T, et al. Drug release from phase-changeable nanodroplets triggered by low-intensity focused ultrasound. *Theranostics*. 2018;8:1327–1339.
68. Desailly Y, Couture O, Fink M, Tanter M. Sono-activated ultrasound localization microscopy. *Appl Phys Lett*. 2013;103:174107.
69. Sheeran PS, Matsunaga TO, Dayton PA. Phase change events of volatile liquid perfluorocarbon contrast agents produce unique acoustic signatures. *Phys Med Biol*. 2014;59:379–401.
70. Christensen-Jeffries K, Couture O, Dayton PA, et al. Super-resolution Ultrasound Imaging. *Ultrasound Med Biol*. 2020;46:865–891.
71. Cerroni B, Cicconi R, Oddo L, et al. In vivo biological fate of poly(vinylalcohol) microbubbles in mice. *Heliyon*. 2018;4:e00770.
72. Paganetti H. *Proton Therapy Physics*. Boca Raton: CRC Press; 2019.
73. Assmann W, Kellnberger S, Reinhardt S, et al. Ionoacoustic characterization of the proton Bragg peak with submillimeter accuracy. *Med Phys*. 2015;42:567–574.
74. Sheeran PS, Yoo K, Williams R, Yin M, Foster FS, Burns PN. More than bubbles: creating phase-shift droplets from commercially available ultrasound contrast agents. *Ultrasound Med Biol*. 2017;43:531–540.
75. Shakya G, Hoff SE, Wang S, Heinz H, Ding X, Borden MA. Vaporizable endoskeletal droplets via tunable interfacial melting transitions. *Sci Adv*. 2020;6:eaaz7188.